Synthetic-reflection self-injection-locked microcombs

Alexander E. Ulanov,[1] Thibault Wildi,[1] Nikolay G. Pavlov,[2]
John D. Jost,[2] Maxim Karpov,[2] Tobias Herr[1,3,*]

[1]Deutsches Elektronen-Synchrotron DESY, Notkestr. 85, 22607 Hamburg, Germany
[2]Enlightra Sarl, Rue de Lausanne 64, 1020 Renens, Switzerland
[3]Physics Department, Universität Hamburg UHH, Luruper Chaussee 149, 22607 Hamburg, Germany
[*]tobias.herr@desy.de

Laser-driven microresonators have enabled chip-integrated light sources with unique properties, including the self-organized formation of ultrashort soliton pulses and frequency combs (microcombs). While poised to impact major photonic applications, such as spectroscopy, sensing and optical data processing, microcombs still necessitate complex scientific equipment to achieve and maintain suitable single-pulse operation. Here, to address this challenge, we demonstrate microresonators with programmable synthetic reflection providing an injection-feedback to the driving laser. When designed appropriately, the synthetic reflection enables robust access to self-injection-locked microcombs operating exclusively in the single-soliton regime and with low-threshold power. These results provide a route to easily-operable microcombs for portable sensors, autonomous navigation, or extreme-bandwidth data processing and represent a novel paradigm that can be generalized to other integrated photonic systems.

Laser-driven microresonators provide access to nonlinear optical phenomena, already with low-power continuous-wave excitation [1]. Leveraging efficient nonlinear frequency conversion, they have enabled novel sources of coherent laser radiation across broad spectral span [2, 3]. Soliton microcombs[4–6] are an important representative of such sources, providing frequency comb spectra of mutually coherent laser lines, based on self-organized dissipative Kerr solitons (DKSs) in resonators with anomalous dispersion [7]. Such DKS microcombs can be integrated on photonic chips [8, 9] and have demonstrated their disruptive potential in many emerging and ground-breaking applications, e.g. high-throughput optical data transmission [10] reaching Pbit-per-second data rates [11], ultrafast laser ranging [12, 13], precision astronomy in support of exo-planet searches [14, 15], high-acquisition rate dual-comb spectroscopy [16], ultra-low noise microwave photonics [17, 18], photonic computing and all-optical neural networks [19–21]. To leverage microcomb technology in out-of-lab applications, it is critical to reliably access the DKS regime and ideally *single*-DKS operation [22], ensuring well-defined temporal and spectral characteristics. While routine in research laboratories, achieving such a state outside such environments is challenging.

A critical challenge lays in the initiation and sustained operation of DKS, requiring the detuning $\Delta\omega_0 = \omega_0 - \omega_\mathrm{p}$ of the pump laser ω_p (with respect to the pumped resonance ω_0) to be controlled and stabilized. While this is common to all resonant approaches, it is particularly challenging during DKS initiation, when thermo-optic effects can cause a rapid ($\sim \mu$s) change in resonance frequency [4]. To overcome this challenge, a number of methods have been developed, involving rapid laser actuation [4, 8], auxiliary lasers [23] and/or auxiliary resonances [24, 25], laser modulation [26], additional nonlinearities [27–29] or, pulsed driving [30]. Many of these methods are now routinely used in research. However, they cannot easily be transferred to out-of-the-lab scenarios, as they require significant experimental skills and scientific instrumentation. In contrast, self-injection locking (SIL) [31–33], has been demonstrated as an approach that can intrinsically follow the rapid changes in resonance frequency and elegantly stabilize the laser detuning for stable DKS operation[17, 34–38]. Usually, SIL is based on Rayleigh backscattering from *random* fabrication imperfections or material defects in the microresonator [39]. The backscattered wave provides feedback (injection) to the driving diode laser and effectively locks the laser frequency to the microresonator. However, backscattering random defects are neither wanted nor can they yield predictable sample characteristics. Relying on random defects is also fundamentally incompatible with the intense efforts towards improved materials and fabrication techniques (targeting material absorption limited performance with negligible scattering similar to optical fiber technology). Already now, fabrication techniques have advanced to a level, where identifying samples with accidental scattering suitable for SIL-based DKS often requires careful and tedious screening.

In this work, we demonstrate SIL and robust access to self-injection locked DKS microcombs *without* relying on random resonator defects. Instead of random backscatter-

ing, we achieve SIL via programmable synthetic reflection, dramatically increasing the access to laser detunings that support DKS. The synthetic reflection is generated via photonic crystal ring resonators (PhCR) [40], which have recently received growing attention in integrated nonlinear photonics [41–45]. In addition, we show that robust access to SIL-based DKS can be combined with recent results of spontaneous single-DKS generation in PhCRs (avoiding non-solitonic states) [41]. Based on analytic criteria, we design the synthetic reflection to ensure exclusive operation in the single-DKS regime as well as low-threshold power. Resulting from the synthetic reflection we also observe DKS breathing [41, 46] in a limited range of operating parameters, which can readily be avoided, if necessary. These results provide a route to easily-operable microcombs for out-of-lab applications.

Results

To gain independence from backscattering random defects and imperfections, we use PhCRs that enable synthetic reflection. The reflection is controlled by periodic nano-patterned corrugations of the ring-resonators' inner walls. The angular corrugation period is $\theta_0 = 2\pi/(2m_0)$, where m_0 is the angular (azimuthal) mode number, for which a deliberate coupling between forward and backward propagating waves with a coupling rate γ is induced (see Fig. 1**a**). Besides inducing the desired synthetic reflection, the coupling leads to mode hybridization resulting in a split resonance lineshape (frequency splitting 2γ) in both transmission and reflection (see Fig. 1**b**). Here, we only consider the lower frequency hybrid mode for pumping, as it corresponds to strong (spectrally local) anomalous dispersion, which prevents high-noise comb states [47]. For choosing γ we balance multiple criteria.

First, a strong reflection can significantly extend the range of normalized detunings $\zeta_0 = 2\Delta\omega_0/\kappa$ (κ is the microresonator linewidth) accessible via SIL (SIL range) in a nonlinear microresonator [37]. This is crucial, as it permits robust access to detunings where DKS can exist (DKS existence range). In conventional resonators the normalized forward-backward coupling is usually small $2\gamma/\kappa < 1$ and the intersection between SIL and DKS ranges is limited to small detunings, complicating access to DKS states. In contrast, strong forward-backward coupling could enable robust access to DKS states over a wide range of detunings. This is exemplified in Fig. 1**c**, where the SIL range [37] is shown along with the conventional analytic DKS existence range (valid for small γ) and the numerically computed DKS existence range for large γ, obtained through numeric integration of the coupled mode equations (cf. Methods). Note, that in a resonator with a shifted pump mode [49], the existence range of DKS deviates strongly from that known from resonators without a shifted pump mode [48] and can currently only be obtained numerically (Fig. 1**c**).

Second, while advantageous for an extended SIL range, stronger forward-backward coupling will also result in an increased parametric threshold (modulation instability,

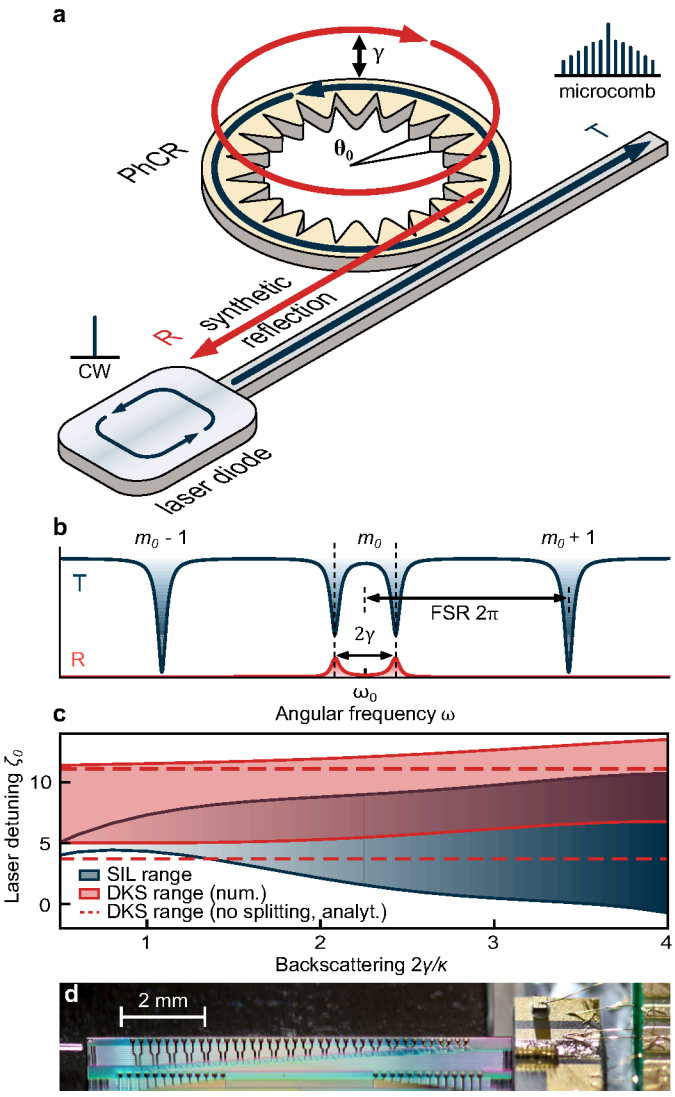

Figure 1 | Self-injection locking with synthetic reflection. **a**, An integrated photonic crystal ring-microresonator (PhCR) with a periodic corrugation (angular period θ_0), which induces coupling at a rate γ between forward and backward-propagating waves for a mode $m_0 = \pi/\theta_0$. In addition to a transmission signal (T), this leads to a well-defined synthetic resonant reflection (R), which can be programmed for self-injection locking with a laser diode driving the system. **b**, Indicative transmission and reflection spectrum for the resonance with mode number m_0 and two adjacent resonances $m_{0\pm1}$, separated by ±1 free-spectral range (FSR). For $\gamma \neq 0$, the lineshape at mode number m_0 exhibits a split lineshape (frequency splitting 2γ), and shows non-zero resonant reflection. **c**, Comparison of nonlinear SIL [37] and DKS existence ranges computed numerically for a critically coupled microresonator with total linewidth $\kappa/2\pi = 120$ MHz, dispersion $D_2/2\pi = 8$ MHz, driven with a normalized pump power of $f^2 = 9$. For large γ, the DKS existence range deviates significantly from the analytical estimation for zero-γ [47, 48]. **d**, Photograph of the experimental system showing the semiconductor laser diode butt-coupled to the photonic chip carrying the PhCRs. Transmitted light is out-coupled using a lensed fiber.

MI) pump power, as detailed in the Supplemental Information (SI). Below this threshold DKS cannot form inside the resonator, without external stimuli (such as triggering pulses [7]). The threshold power is different from that in a conventional ring resonator and its derivation critically requires consideration of the backward wave. For strong forward-backward coupling ($2\gamma/\kappa > 1$), the following approximation is derived (cf. SI):

$$f_{\mathrm{th}}^2 = 4\frac{\gamma}{\kappa} + \frac{\kappa}{\gamma} \tag{1}$$

where $f = \sqrt{8\eta\omega_0 c n_2 P/(\kappa^2 n^2 V_{\mathrm{eff}})}$ is the normalized pump power, with the coupling coefficient $\eta = 1/2$ (critical coupling), ω_0 the resonance frequency of the pumped mode, c the speed of light, P the input pump power, n the refractive index, n_2 the nonlinear refractive index and V_{eff} the effective mode volume. The value of f_{th}^2 must not exceed the available pump power f^2. If the MI threshold is reached at a detuning within the DKS existence range, then the MI state may be only transient and DKS can form spontaneously [41]. In both conventional and pump mode-shifted resonators the DKS regime overlaps with the MI regime and extends further towards larger detunings ζ_0.

Third, with regard to practical applications single-DKS states, as opposed to states with multiple solitons, are highly desirable owing to their smooth squared hyperbolic secant spectral envelope and well-defined temporal output. In their formation process, DKS are seeded by MI, where the separation of the first pair of sidebands from the pump laser in units of the resonator's FSR determines the number of generated DKS [4, 41, 47]. A conservative criterion that guarantees single-DKS formation (i.e. modulation instability sidebands separated from the pump laser by 1 FSR) is derived in the SI:

$$\frac{\gamma}{\kappa} > \frac{f^2}{8} \tag{2}$$

The presented considerations can inform the design of a suitable PhCR for SIL-based DKS.

In preparation of the experiments, a range of critically coupled resonators with varying corrugation amplitude and a free-spectral range (FSR) of 300 GHz (radius 75 µm) are fabricated in a commercial foundry process (Ligentec). We characterize the fabricated resonators via frequency comb-calibrated laser scans [50], permitting to retrieve the coupling rates γ, the resonance widths κ, and the dispersion D_2, over a broad spectral bandwidth. An example is shown in Fig. 2**a**, where indeed the forward-backward coupling is random and $2\gamma/\kappa \ll 1$ for most resonances. In marked contrast, a single pre-defined resonance to which the PhCR's corrugation is matched, exhibits significant forward-backward coupling. Fig. 2**b** shows the dependence of γ and the Q-factor ($Q = \omega_0/\kappa$) on the corrugation amplitude. No noticeable degradation of the Q factor is observed up to $\gamma \lesssim 5$ GHz, and critically coupled linewidth are $\frac{\kappa}{2\pi} \approx 120$ MHz; even for large coupling $\gamma \approx 45$ GHz , the Q-factor is only halved. For the experiments, a semiconductor distributed feedback laser diode (DFB) is butt-coupled to a waveguide on the photonic chip, permitting an estimated on-chip pump power of $P = 30$ mW, corresponding to $f^2 \approx 9$. From Eqs. 1 and 2, we obtain an ideal $2\gamma/\kappa \in (2.26, 4.26)$, ensuring MI-based spontaneous comb initiation and deterministic generation of single DKS. Based on these considerations we choose a PhCR with a synthetic coupling for the pump mode at 1557 nm of $2\gamma/\kappa \approx 4.2$ ($\frac{\gamma}{2\pi} \approx 250$ MHz), within the ideal range. This PhCR is critically coupled and exhibits anomalous group velocity dispersion ($D_2 \approx 8$ MHz). As shown for those values in Fig. 1**c**, numeric simulation confirms that the DKS existence and SIL ranges have significant overlap. We note that another band of DKS existence may exist [49], however, it is inaccessible for spontaneous MI-assisted comb initiation and not considered here. The DFB pump laser diode is mounted on a piezo translation stage to adjust the injection phase [33], an actuator which can readily be achieved through on-chip heaters [38]; to reduce the device footprint and allow for more resonators on the chip, we have omitted this feature. The transmitted light is collected by a lensed-fiber for further analysis as shown in Fig. 2**f**.

In a first experiment, we validate the basic SIL dynamics below parametric threshold at a coupled pump power of 25 mW ($f^2 = 7.3$). As long as the laser diode does not receive a resonant injection from the microresonator it is free running. When the laser's emission wavelength is tuned (via its drive current) close to the lower-frequency pump resonance, a strong resonant backward wave is generated, providing frequency-selective optical feedback resulting in SIL. The SIL regime manifests itself as a rectangular-shaped dip in the transmission signal and, after optimizing the injection phase, extends over a wide range of electrical drive current values. The optical spectrum of the DFB laser in the SIL regime is shown in Fig. 2**e**, showing a single-mode suppression ratio (SMSR) >60 dB. The beatnote of the SIL laser with a table-top low-noise CW laser is shown in Fig. 2**d**. In addition, we record the SIL-laser phase noise (Fig. 2**c**), which is drastically lower than that of the free-running DFB laser diode outside the SIL regime.

In a second experiment, utilizing the same setup as in Fig. 2**f**, we explore DKS-based microcomb generation with the full available pump power (30 mW, $f^2 \approx 9$). Similar to the previous lower power SIL experiment, we slowly (within ca. 10 s) tune the DFB's electrical drive current to scan the emission wavelength across the lower frequency pump resonance, with increasing and then decreasing wavelength. During this scan we monitor the optical spectrum in transmission. We note that the exact tuning curve in the nonlinear SIL regime when increasing (decreasing) the DFB pump current follows a nontrivial behavior that may include non-monotonic sections [37]; the scan outside the SIL range is however monotonic in frequency. Upon entering the SIL regime (again marked

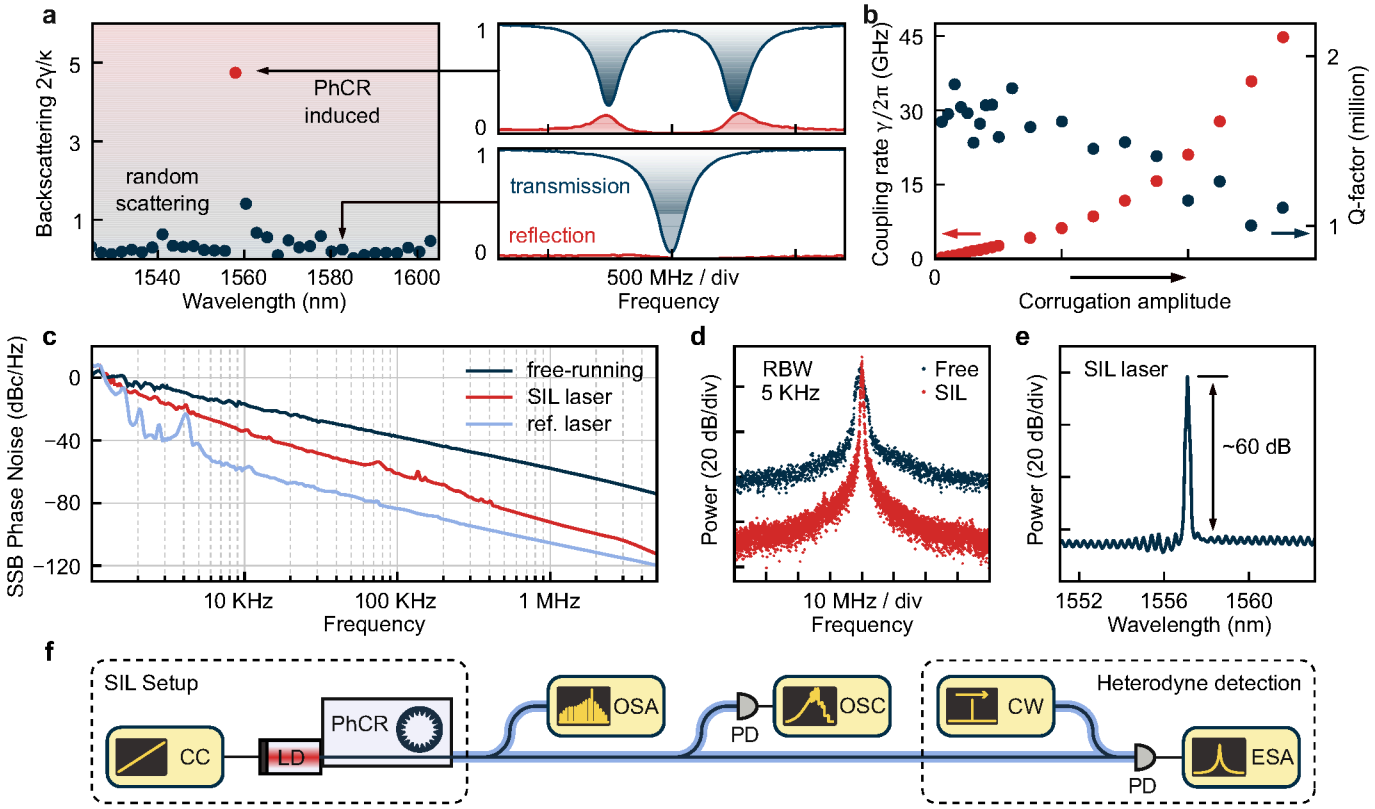

Figure 2 | Resonator characterization and low-power SIL. **a**, The single predefined resonance (red dot) to which the corrugation pattern is matched, exhibits significant forward-backward coupling unlike the other modes (blue dots) where it is weak and random. **b**, Measured forward-backward coupling rates (red, left axis) and Q-factors (blue, right axis) of PhCRs with increasing corrugation amplitude. **c**, Phase noise of the DFB laser in free-running and SIL regimes measured through heterodyne detection with a reference laser. The phase noise of the reference laser is provided as a baseline. **d**, Heterodyne beatnote signal between the reference oscillator and DFB laser in the free-running and SIL states. RBW, resolution bandwidth. **e**, Optical spectrum of the DFB laser in the SIL state. **f**, Experimental setup. CC, current controller; LD, laser diode; OSA and ESA, optical and electrical spectrum analyzers respectively; OSC, oscilloscope; CW, continuous-wave laser; PD, photodiode.

by pronounced dip of the transmitted power after optimization of the injection phase), we observe at first only the single optical frequency of the SIL pump laser, as in the lower power experiment before (Fig. 3**a** ①). Continuing the scan we next observe an abrupt transition into a single-DKS microcomb state (Fig. 3**a** ②). Such single-DKS states are characterized by a smooth squared hyperbolic-secant amplitude and a pulse repetition rate that corresponds to the resonator's FSR; these properties are highly-desirable for applications. Further continuing the scan induces a surprising second abrupt transition into a different single-DKS state (Fig. 3**a** ③). Scanning even further causes the DKS to disappear, with the system returning to CW SIL (spectrum similar to Fig. 3**a** ①), before eventually exiting the SIL regime entirely. When repeated, each scan shows the same SIL dynamics, including deterministic single-DKS generation. Reversing the scan direction qualitatively yields the same phenomena in reversed order. Turing patterns, noisy comb-states and multi-DKS regimes are absent in stark contrast to previous SIL-based microcomb generation, but consistent with spontaneous single-DKS formation in conventionally-driven (non-SIL) PhCR [41]. Although not pursued here, we note that the pump to DKS conversion efficiency in the states ② and ③ is 13.8 % and 15.2 %, resp., significantly higher than what would be expected in conventional resonators. This is a consequence of the mode splitting, shifting the pumped resonance effectively closer to the pump laser as explored previously in coupled ring-resonators [49].

Different from DKS generation experiments in conventionally-driven PhCR, laser tuning speed and even tuning direction are irrelevant and do not noticeably impact the observed dynamics. Owing to the SIL mechanism, switching between the system's states is readily possible and without the risk of 'dropping' out of resonance. Each state of the system can be maintained without requiring external stabilizing feedback. All observations are reproduced in all 4 tested copies of the PhCR (fabricated on 4 different chips). As such, through synthetic reflection, our system not only achieves robust and predictable SIL operation, but also leverages the advantages of spontaneous and deterministic single-DKS generation, observed in conventionally driven PhCRs [41].

To further investigate the SIL dynamics and DKS gen-

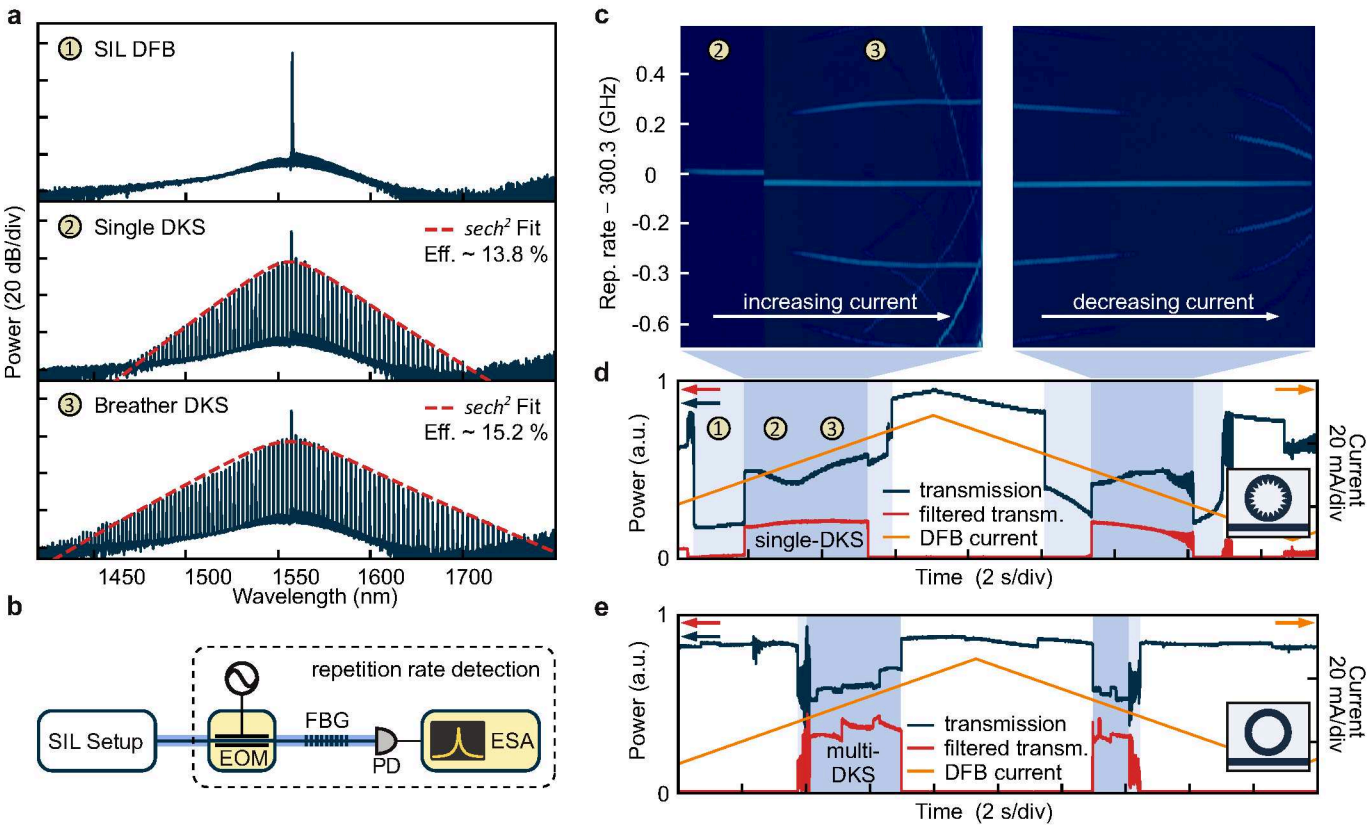

Figure 3 | SIL-based DKS generation. **a**, Optical spectra measured during a laser scan towards longer wavelength within the SIL range: CW SIL ①; SIL-based single DKS states ② and ③. **b**, Experimental setup for repetition rate detection. EOM - electro-optical modulator, FBG - fiber Bragg grating, PD - photodetector, ESA - electrical spectrum analyzer. **c**, Measured SIL-microcomb repetition rate signal representing single DKS ② and breather ③ states. **d** Total transmission (blue) and bandpass-filtered power (red; filter offset from the pump, indicates comb formation) measured during a high-power laser scan with a PhCR. The orange line corresponds to the driving current. **e**, same as **d**, but with a conventional resonator that has been selected for a relatively strong random backscattering (cf. main text for details).

eration, we record the 300 GHz DKS repetition rate beatnote via the setup shown in Fig. 3**b**. As this signal would not be directly detectable, modulation sidebands around a pair of adjacent DKS comb lines are generated electro-optically. Their beating creates a signal at lower frequency, from which the repetition rate can be reconstructed [51]. Fig. 3**c** shows the reconstructed repetition rate signal obtained during the DFB laser scan in both directions. The two distinct spectral regimes are also manifest in this signal: in regime ② a single low-noise repetition rate beatnote is present, whereas in regime ③ additional sidebands (ca. ±200 MHz) indicate a breathing soliton, similar to so far unexplained breathing phenomena in conventionally-driven PhCRs at large detuning [41]. In the wavelength-decreasing scan, the reversed dynamics is observed (the additional breathing towards the end of the scan is well-known from conventionally driven DKS [46]).

During the laser scan, we also record the transmitted power as well as the power of a filtered spectral portion of the long-wavelength wing of the generated microcombs (as an indicator for comb formation). Both are shown along with the DFB diode's drive current in Fig. 3**d**. Here, the SIL regime is clearly evidenced by sharp drops of the (full) transmission from the base level in both scan directions. The DKS regime is marked by the non-zero filtered power within the SIL regime. Note that in Fig. 3**d** the breathing oscillation is only visible in the recorded power for the lowest breathing frequencies, due to the limited 100 MHz bandwidth of the utilized photo-detectors. For comparison, Fig. 3**e** shows a similar transmission and filtered power trace obtained with a *non*-PhCR microresonator of the same FSR. To achieve SIL-based DKS in a non-PhCR, we screened a large number of resonators to find one with large *random* reflection ($2\gamma/\kappa \approx 0.6$) and validated numerically that it can meet the criteria for SIL-based DKS (similar to Fig. 1**c**). In contrast to the PhCR, it does however not respect the criterion for deterministic single-DKS. Indeed, different from the SIL dynamics in the PhCR, noisy comb states before (after) DKS generation are observable in the laser scan and the DKS-regime is dominated by less desirable multi-DKS states, showing the characteristic multi-step features [52]; the single-DKS regime is marginal and only visible as a narrow step when the scan time is reduced to the millisecond level.

To explore the emergence of the breathing soliton at

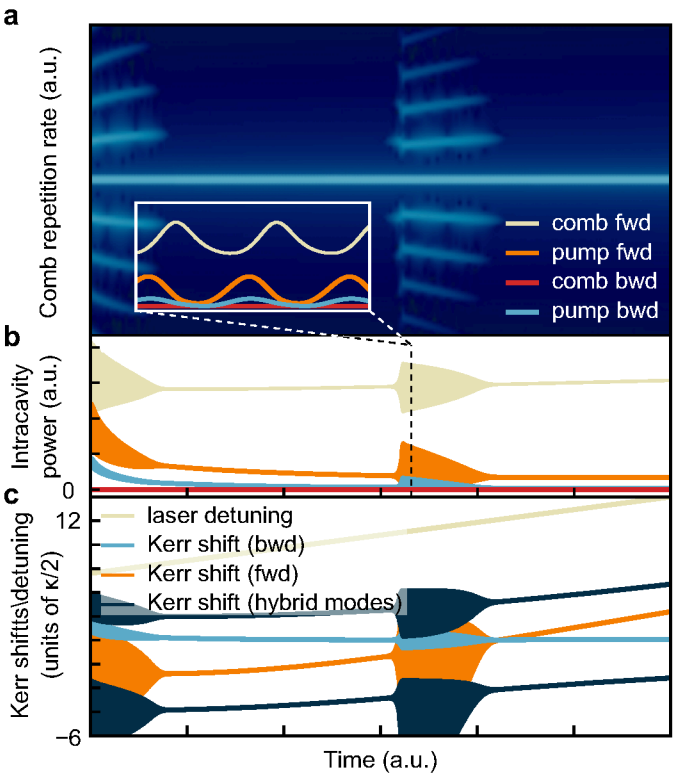

Figure 4 | SIL-microcomb dynamics simulation. **a**, The time-frequency spectrogram reconstructed from the numerical simulation during a wavelength-increasing scan of the pump laser. **b**, Corresponding intracavity powers for forward (beige) and backward (red) propagating microcomb modes ($\mu \neq 0$) as well as forward (orange) and backward (blue) propagating pump modes ($\mu = 0$). **c**, Kerr-shifts of forward (orange) and backward (blue) propagating pump modes with respect to the 'cold' resonance frequency ω_0. Detuning of pump laser (beige). The dark lines indicate the effective hybrid modes frequencies (cf. main text and SI for details).

higher DFB currents (regime ③ in Fig. 3**c,d**), we perform numeric simulation [53, 54], where we include *forward and backward* propagating waves (cf. Methods). Starting from a single DKS state at small detuning (within the well-known breather regime [46]), we integrate the coupled mode equations while imposing a slow laser scan towards longer wavelength. The spectrogram of the repetition rate signal obtained from the numerical simulation is shown in Fig. 4**a**; it reproduces an abrupt appearance of sidebands in agreement with the experimental results of Fig. 3**c**. The average power levels of the pump and comb (full spectrum without pump) in both forward- and backward-direction show rapid oscillations Fig. 4**b**, coinciding with the breathing state. The phase-lag between comb and pump mode suggesting an oscillatory power flow between both, reminiscent of the detuning dependent *intermode breathing* dynamics [55], observed in DKS in the presence of coupling between a DKS mode to a frequency degenerate higher-order transverse mode. The latter is absent in our case, however, by design a strong coupling exists between forward and backward pump modes. Although, up to a certain power level, the strongly coupled forward and backward modes are frequency degenerate numeric simulations suggest that this degeneracy is not generally preserved (similar to CW symmetry breaking [56]) in the DKS regime and dependent on the state of operation. Based on the simulation, we derive the nonlinear frequency shifts of forward and backward propagating pump waves as well as those of the hybridized modes (cf. SI) (Fig. 4**c**). Strikingly, find that the regime of the breathing oscillation coincides with a situation where the differential nonlinear shifts between forward and backward modes are small compared to the resonance width, suggesting forward-backward coupling as its origin. Importantly, the phenomenon is restricted to a specific parameter regime, and can therefore easily be circumvented by choosing the operating parameters (notably pump power or detuning) accordingly.

Conclusion

In conclusion, we have demonstrated microresonators with synthetic reflection for robust SIL and SIL-based microcomb generation. By designing the synthetic reflection we enable deterministic low-threshold, single-DKS operation, highly-favorable for applications and address a major challenge of this technology. For certain combinations of pump power and detuning we observe DKS breathing, which can readily be avoided by small changes in the operating parameters, if necessary. The presented results in conjunction with the scalable, widely accessible fabrication process, the low-cost components, and, notably, its ease of operation meet important requirements of out-of-lab applications and extension to other integrated photonic systems, including normal dispersion combs [52, 57] and novel quantum light sources [58, 59]. Further research may explore extending the presented results to combs in the backward direction (cf. SI) [60], effectively blue-detuned DKS combs with potentially even higher conversion efficiency [49] or multiple pump wavelengths [61].

Materials

Numerical model. To simulate the nonlinear dynamics we consider a system of coupled mode equations [53, 54] for forward a_μ and backward b_μ mode amplitudes, where μ denotes the relative (longitudinal) mode number with respect to the pump mode ($m_0 \leftrightarrow \mu = 0$):

$$\begin{aligned}\partial_t a_\mu =& -(1+i\zeta_\mu)a_\mu + i\sum_{\mu'=\nu+\eta-\mu} a_\nu a_\eta a^*_{\mu'} + 2ia_\mu\sum_\eta |b_\eta|^2 + \\ &+ i\delta_{\mu 0}\frac{2\gamma}{\kappa}b_\mu + f\delta_{\mu 0} \\ \partial_t b_\mu =& -(1+i\zeta_\mu)b_\mu + i\sum_{\mu'=\nu+\eta-\mu} b_\nu b_\eta b^*_{\mu'} + 2ib_\mu\sum_\eta |a_\eta|^2 + \\ &+ i\delta_{\mu 0}\frac{2\gamma}{\kappa}a_\mu\end{aligned}$$

where $\zeta_\mu = \frac{2}{\kappa}(\omega_\mu - \omega_p - \mu D_1)$ is a dimensionless detuning between the pump laser frequency ω_p and cold resonance frequencies $\omega_\mu = \omega_0 + D_1\mu + \frac{1}{2}D_2\mu^2$ (with $D_1/2\pi$ and $D_2/2\pi$

being microresonator FSR and second-order dispersion respectively). The third term in each equation corresponds to the cross-phase modulation by the respective counter-propagating waves, while the fourth term represents the coupling between forward and backward propagating waves. Instead of modeling the SIL dynamics by including laser rate equations, we numerically define the detuning. This approach cannot describe the abrupt transition from the free-running laser to the SIL state, it remains however valid for the specified detuning and can qualitatively capture the features observed in the experiment. Simulation parameters similar to those of the experimental system are used.

Funding

This project has received funding from the European Research Council (ERC) under the EU's Horizon 2020 research and innovation program (grant agreement No 853564), from the EU's Horizon 2020 research and innovation program (grant agreement No 965124) and through the Helmholtz Young Investigators Group VH-NG-1404; the work was supported through the Maxwell computational resources operated at DESY.

Data availability

The datasets generated and analysed during the current study are available from the corresponding author on reasonable request.

Code availability

Numeric simulation codes used in the current study are available from the corresponding author on reasonable request.

Disclosures

The authors declare no competing interests, however disclose that J.D.J. and M.K. are cofounders of Enlightra.

References

1. Vahala, K. J. Optical microcavities. *Nature* **424** (2003).
2. Del'Haye, P. *et al.* Optical frequency comb generation from a monolithic microresonator. *Nature* **450,** 1214–1217 (2007).
3. Sayson, N. L. B. *et al.* Octave-spanning tunable parametric oscillation in crystalline Kerr microresonators. *Nat. Photonics* **13,** 701–706 (2019).
4. Herr, T. *et al.* Temporal solitons in optical microresonators. *Nature Photonics* **8,** 145–152 (2014).
5. Kippenberg, T. J., Gaeta, A. L., Lipson, M. & Gorodetsky, M. L. Dissipative Kerr Solitons in Optical Microresonators. *Science* **361,** eaan8083 (2018).
6. Diddams, S. A., Vahala, K. & Udem, T. Optical frequency combs: Coherently uniting the electromagnetic spectrum. *Science* **369,** eaay3676 (2020).
7. Leo, F. *et al.* Temporal Cavity Solitons in One-Dimensional Kerr Media as Bits in an All-Optical Buffer. *Nature Photonics* **4,** 471–476 (2010).
8. Brasch, V. *et al.* Photonic Chip–Based Optical Frequency Comb Using Soliton Cherenkov Radiation. *Science* **351,** 357–360 (2016).
9. Gaeta, A. L., Lipson, M. & Kippenberg, T. J. Photonic-Chip-Based Frequency Combs. *Nature Photonics* **13,** 158 (2019).
10. Marin-Palomo, P. *et al.* Microresonator-based solitons for massively parallel coherent optical communications. *Nature* **546,** 274–279 (2017).
11. Jørgensen, A. A. *et al.* Petabit-per-Second Data Transmission Using a Chip-Scale Microcomb Ring Resonator Source. *Nature Photonics* **16,** 798–802 (11 2022).
12. Trocha, P. *et al.* Ultrafast Optical Ranging Using Microresonator Soliton Frequency Combs. *Science* **359,** 887–891 (2018).
13. Suh, M.-G. & Vahala, K. J. Soliton Microcomb Range Measurement. *Science* **359,** 884–887 (2018).
14. Suh, M.-G. *et al.* Searching for Exoplanets Using a Microresonator Astrocomb. *Nature Photonics* **13,** 25 (2019).
15. Obrzud, E. *et al.* A microphotonic astrocomb. *Nature Photonics* **13,** 31–35 (2019).
16. Suh, M.-G., Yang, Q.-F., Yang, K. Y., Yi, X. & Vahala, K. J. Microresonator Soliton Dual-Comb Spectroscopy. *Science* **354,** 600–603 (2016).
17. Liang, W. *et al.* High spectral purity Kerr frequency comb radio frequency photonic oscillator. *Nat Commun* **6,** 7957 (2015).
18. Lucas, E. *et al.* Ultralow-Noise Photonic Microwave Synthesis Using a Soliton Microcomb-Based Transfer Oscillator. *Nature Communications* **11,** 374 (1 2020).
19. Feldmann, J. *et al.* Parallel convolutional processing using an integrated photonic tensor core. *Nature* **589,** 52–58 (2021).
20. Xu, X. *et al.* 11 TOPS photonic convolutional accelerator for optical neural networks. *Nature* **589,** 44–51 (2021).
21. Bai, B. *et al.* Microcomb-based integrated photonic processing unit. *Nat Commun* **14,** 66 (2023).
22. Guo, H. *et al.* Universal Dynamics and Deterministic Switching of Dissipative Kerr Solitons in Optical Microresonators. *Nature Physics* **13,** 94–102 (2017).
23. Zhang, S. *et al.* Sub-milliwatt-level microresonator solitons with extended access range using an auxiliary laser. *Optica* **6,** 206–212 (2019).
24. Li, Q. *et al.* Stably accessing octave-spanning microresonator frequency combs in the soliton regime. *Optica* **4,** 193–203 (2017).

25. Weng, H. *et al.* Dual-mode microresonators as straightforward access to octave-spanning dissipative Kerr solitons. *APL Photonics* **7,** 066103 (2022).

26. Wildi, T., Brasch, V., Liu, J., Kippenberg, T. J. & Herr, T. Thermally Stable Access to Microresonator Solitons via Slow Pump Modulation. *Optics Letters* **44,** 4447 (2019).

27. He, Y. *et al.* Self-starting bi-chromatic $LiNbO_3$ soliton microcomb. *Optica* **6,** 1138–1144 (2019).

28. Rowley, M. *et al.* Self-emergence of robust solitons in a microcavity. *Nature* **608,** 303–309 (2022).

29. Bai, Y. *et al.* Brillouin-Kerr Soliton Frequency Combs in an Optical Microresonator. *Physical Review Letters* **126,** 063901 (2021).

30. Obrzud, E., Lecomte, S. & Herr, T. Temporal Solitons in Microresonators Driven by Optical Pulses. *Nature Photonics* **11,** 600–607 (2017).

31. Vasil'ev, V. V. *et al.* High-Coherence Diode Laser with Optical Feedback via a Microcavity with 'whispering Gallery' Modes. *Quantum Electronics* **26,** 657 (1996).

32. Liang, W. *et al.* Whispering-gallery-mode-resonator-based ultranarrow linewidth external-cavity semiconductor laser. *Opt. Lett.* **35,** 2822–2824 (2010).

33. Kondratiev, N. M. *et al.* Self-injection locking of a laser diode to a high-Q WGM microresonator. *Optics Express* **25,** 28167 (2017).

34. Pavlov, N. G. *et al.* Narrow-linewidth lasing and soliton Kerr microcombs with ordinary laser diodes. *Nature Photonics* **12,** 694–698 (2018).

35. Raja, A. S. *et al.* Electrically pumped photonic integrated soliton microcomb. *Nature Communications* **10,** 680 (2019).

36. Shen, B. *et al.* Integrated turnkey soliton microcombs. *Nature* **582,** 365–369 (2020).

37. Voloshin, A. S. *et al.* Dynamics of soliton self-injection locking in optical microresonators. *Nature Communications* **12,** 235 (2021).

38. Xiang, C. *et al.* Laser soliton microcombs heterogeneously integrated on silicon. *Science* **373,** 99–103 (2021).

39. Gorodetsky, M. L., Pryamikov, A. D. & Ilchenko, V. S. Rayleigh Scattering in High-Q Microspheres. *JOSA B* **17,** 1051–1057 (2000).

40. Arbabi, A., Kang, Y. M., Lu, C.-Y., Chow, E. & Goddard, L. L. Realization of a narrowband single wavelength microring mirror. *Appl. Phys. Lett.* **99,** 091105 (2011).

41. Yu, S.-P. *et al.* Spontaneous pulse formation in edgeless photonic crystal resonators. *Nature Photonics* **15,** 461–467 (2021).

42. Lu, X., McClung, A. & Srinivasan, K. High-Q slow light and its localization in a photonic crystal microring. *Nature Photonics* **16,** 66–71 (2022).

43. Black, J. A. *et al.* Optical-parametric oscillation in photonic-crystal ring resonators. *Optica* **9,** 1183 (2022).

44. Yang, K. Y. *et al.* Multi-dimensional data transmission using inverse-designed silicon photonics and microcombs. *Nat Commun* **13,** 7862 (2022).

45. Lucas, E., Yu, S.-P., Briles, T. C., Carlson, D. R. & Papp, S. B. *Tailoring microcombs with inverse-designed, meta-dispersion microresonators* arXiv:2209.10294. 2022.

46. Lucas, E., Karpov, M., Guo, H., Gorodetsky, M. L. & Kippenberg, T. J. Breathing dissipative solitons in optical microresonators. *Nat Commun* **8,** 736 (2017).

47. Herr, T. *et al.* Universal formation dynamics and noise of Kerr-frequency combs in microresonators. *Nature Photonics* **6,** 480–487 (2012).

48. Godey, C., Balakireva, I. V., Coillet, A. & Chembo, Y. K. Stability Analysis of the Spatiotemporal Lugiato-Lefever Model for Kerr Optical Frequency Combs in the Anomalous and Normal Dispersion Regimes. *Physical Review A* **89** (2014).

49. Helgason, Ó. B. *et al.* Power-efficient soliton microcombs. arXiv:2202.09410 (2022).

50. Del'Haye, P., Arcizet, O., Gorodetsky, M. L., Holzwarth, R. & Kippenberg, T. J. Frequency Comb Assisted Diode Laser Spectroscopy for Measurement of Microcavity Dispersion. *Nature Photonics* **3,** 529–533 (2009).

51. Del'Haye, P., Papp, S. B. & Diddams, S. A. Hybrid Electro-Optically Modulated Microcombs. *Physical Review Letters* **109,** 263901 (2012).

52. Lihachev, G. *et al.* Platicon microcomb generation using laser self-injection locking. *Nat Commun* **13,** 1771 (2022).

53. Chembo, Y. K. & Yu, N. Modal expansion approach to optical-frequency-comb generation with monolithic whispering-gallery-mode resonators. *Physical Review A* **82,** 033801 (2010).

54. Hansson, T., Modotto, D. & Wabnitz, S. On the numerical simulation of Kerr frequency combs using coupled mode equations. *Optics Communications* **312,** 134–136 (2014).

55. Guo, H. *et al.* Intermode Breather Solitons in Optical Microresonators. *Phys. Rev. X* **7,** 041055 (2017).

56. Del Bino, L., Silver, J. M., Stebbings, S. L. & Del'Haye, P. Symmetry Breaking of Counter-Propagating Light in a Nonlinear Resonator. *Scientific Reports* **7,** 43142 (1 2017).

57. Xue, X., Qi, M. & Weiner, A. M. Normal-dispersion microresonator Kerr frequency combs. *Nanophotonics* **5,** 244–262 (2016).

58. Zhao, Y. *et al.* Near-Degenerate Quadrature-Squeezed Vacuum Generation on a Silicon-Nitride Chip. *Physical Review Letters* **124,** 193601 (2020).

59. Lu, H.-H. *et al.* Bayesian tomography of high-dimensional on-chip biphoton frequency combs with randomized measurements. *Nat Commun* **13,** 4338 (2022).

60. Fujii, S. *et al.* Effect on Kerr comb generation in a clockwise and counter-clockwise mode coupled microcavity. *Opt. Express* **25,** 28969 (2017).

61. Chermoshentsev, D. A. *et al.* Dual-laser self-injection locking to an integrated microresonator. *Optics Express* **30,** 17094 (2022).

Synthetic-self-injection locked microcombs - Supplemental Information

Alexander E. Ulanov,[1] Thibault Wildi,[1] Nikolay G. Pavlov,[2]
John D. Jost,[2] Maxim Karpov,[2] Tobias Herr[1,3,*]

[1]Deutsches Elektronen-Synchrotron DESY, Notkestr. 85, 22607 Hamburg, Germany
[2]Enlightra Sarl, Rue de Lausanne 64, 1020 Renens, Switzerland
[3]Physics Department, Universität Hamburg UHH, Luruper Chaussee 149, 22607 Hamburg, Germany
*tobias.herr@desy.de

1 Coupled mode equations and pump mode hybridization

The normalized coupled mode equations (CMEs) for the pump in forward and backward directions read

$$\partial_t a_0 = -(1+i\zeta_0)a_0 + i|a_0|^2 a_0 + 2i|b_0|^2 a_0 + i\beta b_0 + f \tag{1}$$

$$\partial_t b_0 = -(1+i\zeta_0)b_0 + i|b_0|^2 b_0 + 2i|a_0|^2 b_0 + i\beta a_0 \tag{2}$$

where for convenience the normalized coupling rate $\beta = 2\gamma/\kappa \geq 0$ has been introduced. Without loss of generality, $f \geq 0$.

The coefficient matrix of the system of equations (without the pump)

$$M = \begin{pmatrix} -(1+i\zeta_0) + i|a_0|^2 + 2i|b_0|^2 & i\beta \\ i\beta & -(1+i\zeta_0) + i|b_0|^2 + 2i|a_0|^2 \end{pmatrix} \tag{3}$$

has the following Eigenvalues

$$\lambda_\pm = -\left(1 + i\zeta_0 - \frac{3}{2}i(|a_0|^2 + |b_0|^2) \pm i\sqrt{\beta^2 + \left(\frac{1}{2}(|a_0|^2 - |b_0|^2)\right)^2}\right) \tag{4}$$

$$= -\left(1 + i(\zeta_0 - \delta\zeta_{\mathrm{NL}} \pm \sqrt{\beta^2 + \delta\beta_{\mathrm{NL}}^2})\right) \tag{5}$$

and is diagonalized in the following Eigenbasis of hybridized forward-backward modes

$$\left\{\frac{1}{2}(|a_0|^2 - |b_0|^2) \pm \sqrt{\beta^2 + \left(\frac{1}{2}(|a_0|^2 - |b_0|^2)\right)^2};\ -\beta\right\} \tag{6}$$

$$= \left\{\delta\beta_{\mathrm{NL}} \pm \sqrt{\beta^2 + \delta\beta_{\mathrm{NL}}^2};\ -\beta\right\} \tag{7}$$

where $\delta\beta_{\mathrm{NL}} = \frac{1}{2}(|a_0|^2 - |b_0|^2)$ and $\delta\zeta_{\mathrm{NL}} = \frac{3}{2}(|a_0|^2 + |b_0|^2)$. The transformation matrices are:

$$T = \begin{pmatrix} \delta\beta_{\mathrm{NL}} + \sqrt{\beta^2 + \delta\beta_{\mathrm{NL}}^2} & \delta\beta_{\mathrm{NL}} - \sqrt{\beta^2 + \delta\beta_{\mathrm{NL}}^2} \\ -\beta & -\beta \end{pmatrix} \tag{8}$$

and

$$T^{-1} = \begin{pmatrix} \frac{1}{2\sqrt{\beta^2 + \delta\beta_{\mathrm{NL}}^2}} & \frac{\delta\beta_{\mathrm{NL}} - \sqrt{\beta^2 + \delta\beta_{\mathrm{NL}}^2}}{2\beta\sqrt{\beta^2 + \delta\beta_{\mathrm{NL}}^2}} \\ -\frac{1}{2\sqrt{\beta^2 + \delta\beta_{\mathrm{NL}}^2}} & \frac{-\delta\beta_{\mathrm{NL}} - \sqrt{\beta^2 + \delta\beta_{\mathrm{NL}}^2}}{2\beta\sqrt{\beta^2 + \delta\beta_{\mathrm{NL}}^2}} \end{pmatrix} \tag{9}$$

so that

$$\begin{pmatrix} a_0 \\ b_0 \end{pmatrix} = T \begin{pmatrix} a_+ \\ a_- \end{pmatrix} \tag{10}$$

and

$$\begin{pmatrix} a_+ \\ a_- \end{pmatrix} = T^{-1} \begin{pmatrix} a_0 \\ b_0 \end{pmatrix} \tag{11}$$

where $a_\pm$ denote the (not specifically normalized) field amplitudes of the hybrid modes. The steady state equations for the hybrid modes are

$$0 = -\left(1 + i(\zeta_0 - \delta\zeta_{\mathrm{NL}} + \sqrt{\beta^2 + \delta\beta_{\mathrm{NL}}^2})\right) a_+ + \frac{1}{2\sqrt{\beta^2 + \delta\beta_{\mathrm{NL}}^2}} f \tag{12}$$

$$0 = -\left(1 + i(\zeta_0 - \delta\zeta_{\mathrm{NL}} - \sqrt{\beta^2 + \delta\beta_{\mathrm{NL}}^2})\right) a_- - \frac{1}{2\sqrt{\beta^2 + \delta\beta_{\mathrm{NL}}^2}} f \tag{13}$$

In non-normalized units, the effective resonance frequencies of the hybridized modes are

$$\omega_{\pm,\mathrm{eff}} = \omega_0 - \frac{\kappa}{2}\left(\delta_{\mathrm{NL}} \pm \sqrt{\beta^2 + \delta\beta_{\mathrm{NL}}^2}\right) \tag{14}$$

2 Approximations for the forward pump mode under strong coupling

In what follows, it is assumed that

- the coupling is strong $\beta > 1$
- due to the strong coupling, the power levels in forward and backward directions are approximately equal $|a_0|^2 = |b_0|^2$. Note that due to symmetry breaking [56] this is only valid up to a certain power level. We validated, by numeric integration of the CMEs 1 and 2, that this approximation is valid.
- the detuning ζ_0 is such that approximately only the lower frequency hybrid mode a_- is driven, i.e. $|a_-| \gg |a_+|$.

Under these assumptions,

$$a_0 = \left(\delta\beta_{\mathrm{NL}} - \sqrt{\beta^2 + \delta\beta_{\mathrm{NL}}^2}\right) a_- \approx -\beta a_- \tag{15}$$

$$b_0 = -\beta a_- \tag{16}$$

and in consequence

$$(1 + i(\zeta_0 - \delta\zeta_{\mathrm{NL}} - \beta))a_0 = \frac{f}{2} \tag{17}$$

Multiplying each side of the equation with its complex conjugate results in

$$(1 + (\zeta_0 - \delta\zeta_{\mathrm{NL}} - \beta)^2)|a_0|^2 = \frac{f^2}{4} \tag{18}$$

An immediate insight is that the strong coupling between forward and backward waves limits the power in the forward (or backward) wave to values of

$$|a_0|^2 \leq f^2/4 \tag{19}$$

Expressing $\delta\zeta_{\mathrm{NL}}$ via the field amplitudes gives

$$(1 + (\zeta_0 - 3|a_0|^2 - \beta)^2)|a_0|^2 = \frac{f^2}{4} \tag{20}$$

and for the detuning

$$\zeta_{0,\pm} = \beta + 3|a_0|^2 \pm \sqrt{\frac{f^2}{4|a_0|^2} - 1} \tag{21}$$

where $\zeta_{0,+}$ corresponds to an effective red-detuning and $\zeta_{0,-}$ to an effective blue-detuning with regard to the lower-frequency hybrid mode a_-.

3 Threshold condition and first oscillating sideband

We consider two initially zero-power (except for vaccuum fluctuations) sidebands with mode number $\pm\mu$ relative to the pumped mode. Their CMEs are

$$\partial_t a_{+\mu} = -(1 + i(\zeta_\mu - 4|a_0|^2))a_{+\mu} + ia_0^2 a_{-\mu}^* \tag{22}$$

$$\partial_t a_{-\mu}^* = -(1 - i(\zeta_\mu - 4|a_0|^2))a_{-\mu}^* - ia_0^{*2} a_{+\mu} \tag{23}$$

where again $|a_0|^2 \approx |b_0|^2$ was assumed and $\zeta_\mu = \frac{2}{\kappa}(\omega_0 - \omega_\mathrm{p} + \frac{1}{2}D_2\mu^2) = \zeta_0 + \frac{D_2}{\kappa}\mu^2$. The Eigenvalues of this set of equations are

$$\lambda_\pm = -1 \pm \sqrt{|a_0|^4 - (\zeta_\mu - 4|a_0|^2)^2} \tag{24}$$

The parametric gain experienced by the two sidebands therefore is

$$G = \kappa\sqrt{|a_0|^4 - \left(\zeta_0 + \frac{D_2}{\kappa}\mu^2 - 4|a_0|^2\right)^2} \tag{25}$$

At least a intracavity power of $|a_0|^2 = 1$ is required to reach threshold. With Eq. 19 it follows that for strong coupling the threshold pump power $f^2 \geq 4|a_0|$ is at least four times the threshold power of a resonator without forward-backward coupling.

3.1 First oscillating sideband

The phase mismatch between the pump wave and the resonator modes can be quantified via their effective (including nonlinear frequency shifts) detuning $\zeta_{\mu,\mathrm{eff}}$ from an equidistant D_1-space frequency grid. A smaller $\zeta_{\mu,\mathrm{eff}}$ implies better phase matching.

$$\zeta_{\mu,\mathrm{eff}} = \zeta_0 + \frac{D_2}{\kappa}\mu^2 - 4|a_0|^2 \tag{26}$$

$$= \beta - |a_0|^2 \pm \sqrt{\frac{f^2}{4|a_0|^2} - 1} + \frac{D_2}{\kappa}\mu^2 \tag{27}$$

For DKS the resonator is characterized by anomalous dispersion $D_2 > 0$ ($\beta \gg D_2/\kappa$). It can therefore be guaranteed, that the first generated sideband pair (best phase matching) will be $\mu \pm 1$, if

$$\beta - |a_0|^2 - \sqrt{\frac{f^2}{4|a_0|^2} - 1} > 0 \tag{28}$$

Assuming $|a_0|^2 \leq f^2/4$ we find

$$\boxed{\beta > f^2/4 \quad \Leftrightarrow \quad \gamma/\kappa > f^2/8} \tag{29}$$

as a condition that guarantees that the first sideband pair will be generated at $\mu = \pm 1$.

3.2 Threshold power

The threshold power f_th is the power level where the parametric threshold $G > \kappa$ can be reached. Inserting Eq. 21 for the detuning into Eq. 25, we obtain for the threshold condition

$$|a_0|^4 - \left(\beta + 3|a_0|^2 \pm \sqrt{\frac{f_\mathrm{th}^2}{4|a_0|^2} - 1} + \frac{D_2}{\kappa}\mu^2 - 4|a_0|^2\right)^2 = 1 \tag{30}$$

$$\Leftrightarrow |a_0|^4 - 1 = \left(\beta \pm \sqrt{\frac{f_\mathrm{th}^2}{4|a_0|^2} - 1} + \frac{D_2}{\kappa}\mu^2 - |a_0|^2\right)^2 \tag{31}$$

Under the assumption that $\beta - |a_0|^2 - \sqrt{\frac{f_\mathrm{th}^2}{4|a_0|^2} - 1} > 0$ (condition for first oscillating sidebands $\mu = \pm 1$), this results in

$$\boxed{f_\mathrm{th}^2 = 4|a_0|^2 + 4|a_0|^2\left(\beta - |a_0|^2 + \frac{D_2}{\kappa}\mu^2 - \sqrt{|a_0|^4 - 1}\right)^2, \quad (|a_0|^4 > 1)} \tag{32}$$

This equation can be solved numerically. For example, $\beta = 4$ results in $f_\mathrm{th}^2 \approx 8.4$

3.3 Threshold power assuming zero-effective detuning

A simplified threshold condition may be derived assuming that the threshold will be reached at zero effective detuning so that

$$\zeta_0 = \beta + 3|a_0|^2 \qquad \text{and} \tag{33}$$

$$f_{\mathrm{th}}^2 = 4|a_0|^2 \tag{34}$$

In this case the threshold condition is

$$|a_0|^4 - \left(\beta + 3|a_0|^2 + \frac{D_2}{\kappa}\mu^2 - 4|a_0|^2\right)^2 = 1 \tag{35}$$

$$\Leftrightarrow \frac{f_{\mathrm{th}}^4}{16} - \left(\beta - \frac{1}{4}f_{\mathrm{th}}^2 + \frac{D_2}{\kappa}\mu^2\right)^2 = 1 \tag{36}$$

$$\Leftrightarrow f_{\mathrm{th}}^2 = \frac{2 + 2\left(\beta + \frac{D_2}{\kappa}\mu^2\right)^2}{\beta + \frac{D_2}{\kappa}\mu^2} \tag{37}$$

Assuming that $\beta \gg \frac{D_2}{\kappa}\mu^2$ this simplifies to

$$\boxed{f_{\mathrm{th}}^2 \approx \frac{2 + 2\beta^2}{\beta} = 2\beta + \frac{2}{\beta} \quad \Leftrightarrow \quad f_{\mathrm{th}}^2 \approx 4\frac{\gamma}{\kappa} + \frac{\kappa}{\gamma}} \tag{38}$$

For $\beta = 4$ we find $f_{\mathrm{th}}^2 = 8.5$, almost equal to what is obtained through Eq. 32.

4 Pump mode hybridization above threshold

The derivations of Section 1 are only valid below threshold, where only the forward and backward pump mode are excited. Above threshold, and in particular in presence of DKS, the effective frequencies of the hybrid mode resulting from the avoided mode crossing of the coupled forward and backward modes are

$$\omega_{\pm,\mathrm{eff}} = \frac{1}{2}(\omega_{\mathrm{a,eff}} + \omega_{\mathrm{b,eff}}) + \frac{1}{2}\sqrt{(\omega_{\mathrm{a,eff}} - \omega_{\mathrm{b,eff}})^2 + 4\gamma^2} \tag{39}$$

where $\omega_{\mathrm{a,eff}}$ and $\omega_{\mathrm{b,eff}}$ are the effective (i.e. taking nonlinear frequency shifts into account) resonance frequencies of the forward and backward modes, respectively.

$$\omega_{\mathrm{a,eff}} = \omega_0 - \frac{\kappa}{2}\left(\mathrm{Re}(\hat{\mathcal{F}}[|\psi_a(\theta)|^2\psi_a(\theta)]_{\mu=0}/a_0) + 2\sum_\eta |b_\eta|^2\right) \tag{40}$$

$$\omega_{\mathrm{b,eff}} = \omega_0 - \frac{\kappa}{2}\left(\mathrm{Re}(\hat{\mathcal{F}}[|\psi_b(\theta)|^2\psi_b(\theta)]_{\mu=0}/b_0) + 2\sum_\eta |a_\eta|^2\right) \tag{41}$$

$$\tag{42}$$

where $\psi_a(\theta) = \hat{\mathcal{F}}^{-1}[a_\mu]$ and $\psi_b(\theta) = \hat{\mathcal{F}}^{-1}[b_\mu]$ are the spatio-temporal field profiles and $\hat{\mathcal{F}}[\ .\ ]_0$ stands for the component corresponding to the pump mode ($\hat{\mathcal{F}}$ denotes the Fourier transform).

5 Comb generation in the backward direction

Due to the initially similar power-levels in forward and backward pump modes, combs may in principle not only be generated in the forward, but also in the backward direction. Indeed, when the pump laser detuning is between the (effective) resonance frequencies of the hybridized modes, the backward-wave is usually stronger (despite the forward-pumping). For the parameters considered in this work, we found that this range of detuning does not overlap with the soliton existence range and backward combs were not observed. However, backward combs represent an interesting opportunity for additional research. Aside from backward comb generation we note, that backward modulation instability, can trigger forward modulation instability (and comb generation) and vice versa, through a non-zero forward-backward coupling of the modulation instability sidebands. This can readily be included in the numeric model by introducing non-zero γ also for modes with $\mu \neq 0$.